Design and Control Methodology of a Three-Port Resonant Converter for Electric Vehicles

NILOUFAR KESHMIRI (Student Member, IEEE),
GUVANTHI ABEYSINGHE MUDIYANSELAGE (Student Member, IEEE),
SREEJITH CHAKKALAKKAL (Student Member, IEEE), **KYLE KOZIELSKI** (Student Member, IEEE),
GIORGIO PIETRINI (Member, IEEE), **AND ALI EMADI** (Fellow, IEEE)

McMaster Institute for Automotive Research and Technology, McMaster University, Hamilton, ON L8P 0A6, Canada

CORRESPONDING AUTHOR: NILOUFAR KESHMIRI (e-mail: keshmin@mcmaster.ca)

ABSTRACT Three-port converters (TPCs) enable the design of more efficient, power dense,and high-power dc–dc converters. This article investigates the operation of a resonant TPC in electric vehicle applications. Operating conditions of the resonant TPC are presented. The steady-state analysis of the converter with zero-voltage switching consideration is discussed. A controller concept to regulate the resonant TPC is proposed. State-space equations of the resonant TPC are derived, and a nested closed-loop control strategy is implemented. The converter operation is validated in the PLECS simulation environment under step-load and input voltage variation conditions. The resonant TPC can regulate its output voltage under the proposed control strategy and maintain its operation at various operating conditions.

INDEX TERMS DC–DC converter, electric vehicle (EV), lookup table, three-port converter (TPC), zero-voltage switching (ZVS).

I. INTRODUCTION

With increasing demand for environmentally friendlier vehicles with higher fuel economy, the trend toward electric vehicles (EVs) has increased significantly in recent years [1]. To meet the electrical power demands for these vehicles, the use of electronic systems to improve the EV performance, efficiency, emissions, and passenger comfort is necessary. Specifically, the power electronics and electric machines in EVs need to be designed to obtain high efficiency, high power density, and low costs [2].

In EVs, multiple dc–dc converters are used for power conversion [3]. These converters require galvanic isolation via a transformer, due to the large conversion ratios between the source and load buses.

The different buses within an EV that require power conversion are the source, battery, and the dc bus (load). A dc–dc converter is required to interface the source and the dc bus with a second converter used for conversion between the battery and the dc bus [4]. Each dc–dc converter has its own controller, determining the power sharing ratio. To improve power density and enhance system efficiency, the use of a single-stage conversion is beneficial.

Multi-input dc–dc converters combine different energy systems, particularly in renewable energy sources and hybrid EVs [5], [6]. EVs typically have multiple energy storage systems (ESSs) such as the batteries and ultracapacitors. Multiport converters permit the interface of the converter with multiple ESSs, using a single-stage power conversion as opposed to connecting multiple converters in series and/or parallel [7]. A centralized controller is used to regulate the output voltage and obtain the power sharing ratio [4]. The multiport converter is desirable in high-power applications through the interface of multiple sources with the load [8]. Multiport converters use single-stage ac-link power conversion instead of multiple power conversion stages. In EV applications, multiport isolated converters (MPICs) permit the

energy captured during regenerative braking to flow back to the source, resulting in increased efficiency [2]. Therefore, bidirectional power transfer is desirable in EVs.

The MPIC, however, faces challenges such as increased weight and volume due to a higher number of switches with larger transformers. The control of multiple switches also becomes challenging. The MPIC topology and its control strategy must be investigated to fully exploit the benefits offered by these converters.

Among the different three-port converter (TPC) topologies, the triple active bridge (TAB), half-bridge, and resonant three-port converters (RTPCs) are the most common.

A three-port three-phase dc–dc converter is presented in [9]. Replacing the single-phase bridge with a three-phase bridge permits higher power operation. However, the three-phase system has more semiconductors, passive components, and a larger and more complex transformer. The control of the three-port three-phase converter becomes challenging.

A 750-W TPC formed by the integration of a nonisolated bidirectional dc–dc converter (NBC) and a dual-active-bridge (DAB) converter is proposed in [10]. The nonisolated port corresponds to the 12-V battery with the 48-V and high-voltage (HV) battery represented by ports 1 and 2, respectively. The proposed topology has an efficiency of 90% at low power. With demand for more efficient converters and the trend toward electrification, the design of high-power converters is necessary. The NBC-DAB topology is, therefore, not suitable for high-power applications.

A 500-W fuel cell/battery hybrid system is proposed in [11]. The proposed system enhances the transient response of a polymer electrolyte membrane fuel cell stack. An energy management system is developed to compensate for fast load variations with a feedforward control that distributes the energy between the different ports. The proposed energy management system improves converter dynamics. However, at higher power levels, the implementation of the strategy is challenging.

A 1-kW TAB converter is presented in [12]. Through phase shifting between the bridges, the direction of power flow is determined [12]. The fuel cell, load, and supercapacitor are represented by ports 1, 2, and 3, respectively. A 3-kW TAB converter with the fuel cell, load, and supercapacitor configuration is proposed in [7]. With duty cycle control, the efficiency of the converter is improved due to the extension of the zero-voltage switching (ZVS) range. Duty ratio control ensures ZVS at all operating conditions [7]. One drawback of the TAB is the dependence of the switching frequency on the inductor value at the same power [4]. At medium-to-high-power conditions, the inductance becomes difficult to control. To allow controllability, the leakage inductance must increase.

Since the inductance is inversely proportional to the switching frequency, the increase of the leakage inductance lowers the frequency, which affects power density. To overcome this issue, a series RTPC is proposed in [4]. The resonant converter enables the reduction of the peak current with near sinusoidal voltages and currents, while simplifying the controller design.

Peak current reduction lowers the demand on the transformer, enabling the use of smaller magnetics and filters. The reduction of the current stress also lowers losses, improving efficiency.

The leakage inductor in the RTPC aids in power flow and controllability, independent of the switching frequency. Series-resonant converters are attractive candidates for high-power dc–dc converter applications because of their wide soft-switching range, reduced electromagnetic interference (EMI), and reduced switching losses [13]. In a resonant converter, the port currents are nearly sinusoidal. Hence, by proper design and control, the converter can be switched near the zero-crossing intervals, which makes the converter switch at even higher frequencies and reduces the EMI. It further reduces the size of resonant tank elements and improves the power density in the range of conventional TPCs. Owing to these superior properties offered by the RTPC, the control and operation of the RTPC will be investigated in this article.

With the trend toward HV batteries in EVs, the use of highly efficient dc–dc converters becomes necessary. Currently, the HV battery in EVs is operating at 800 V. The goal is to increase the voltage level to 1200 V in the near future. HV operation is desirable since it increases power levels, while maintaining high efficiencies, at lower current values.

The low-voltage (LV) battery in the EV is at 12 and 48 V. The conversion ratio between the HV and LV batteries is large and, therefore, requires a robust controller. The HV batteries are also typically larger in size. Therefore, it is important for the dc–dc converters in the vehicle to be as power dense as possible, to maintain passenger comfort. The RTPC offers an efficient and power dense solution. Most of the previous works on RTPCs have been implemented at low power levels. With EV batteries going to higher voltages, the design of high-power converters becomes necessary. A step-by-step design methodology of the RTPC with detailed control system design and analysis is lacking. In this article, the design of a 6-kW RTPC is presented in detail. State-space equations of the RTPC are derived, and the governing equations representing the RTPC are presented. A nested control loop strategy is proposed and validated through simulations to regulate the converter under varying load conditions. The proposed methodology can be extended to any resonant converter operating at various bus voltages, for different applications.

The rest of this article is organized as follows. Section II covers the RTPC topology overview, modes of operation, and the control strategy. The steady-state analysis of the RTPC along with its power flow equations and soft switching operation is discussed in Section III. The control design is presented in Section IV with state-space equation derivations. The decoupling network and the closed-loop control strategy used for the RTPC are investigated. Section V covers simulation results of the proposed controller, implementing the control technique in the PLECS simulation environment. The results are validated in a closed-loop controller through the step-load and input voltage variation tests. Finally, Section VI concludes this article.
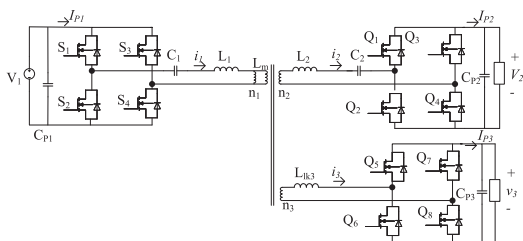
FIGURE 1. Three-port resonant converter topology.

FIGURE 2. Operating modes of the RTPC.

II. THREE-PORT RESONANT CONVERTER

The configuration of the resonant tank in resonant converters can be either series, parallel, or series–parallel. A fully isolated RTPC topology with two series resonant tanks is proposed in [4]. With the series resonant tanks, this converter can operate only in buck operation. Another topology with two multielement series–parallel resonant tanks is proposed in [14]. Coupling among the three ports is challenging in the controller design of TPCs. As a solution, a hardware decoupled RTPC with series resonant tanks is proposed in [15]. However, in proposed RTPC, wide operating voltage and load range are not considered, and bidirectional power flow capability between any two or three ports is not discussed. In this article, the design and control of an isolated bidirectional RTPC topology is proposed, considering a wide voltage range for the three ports.

A. TOPOLOGY OVERVIEW

The RTPC is shown in Fig. 1 [11]. Port 1 is considered to be the HV port, and ports 2 and 3 are the medium-voltage and LV ports, respectively. The port 1, port 2, and port 3 voltages are defined as V_1, V_2, and V_3, respectively. The converter operates under a wide voltage range for the three ports: $V_1 = [400$ V 600 V 800 V], $V_2 = [46$ V 48 V 50 V], and $V_3 = [10$ V 12 V 14 V]. The use of metal–oxide–semiconductor field-effect transistors on the three bridges ensures bidirectional power flow between any two ports. The RTPC discussed in this work consists of two series resonant tanks with C_1, L_1 and C_2, L_2. For control simplicity, a phase-shift and duty ratio control strategy at a fixed switching frequency (f_s) was selected. Therefore, both the resonant tanks are designed at a single resonant frequency (f_r). Ports 1 and 2 have resonant tanks; however, it is excluded in port 3. In the current application, port 3 is a high-power LV port, with higher current levels compared to ports 1 and 2. The energy stored in the port 3 parasitic inductance is sufficiently large to instantaneously discharge the inverter output capacitance for soft switching [16]. This eliminates the need for a dedicated resonant tank for port 3 while preventing the need for a large inductor. An *LLC* resonant tank with the magnetizing inductance (L_m) is considered to provide buck and boost mode operation. The leakage inductance of port 3 (L_{lk3}) is also modeled in the topology to represent the ac impedance of the port as it does no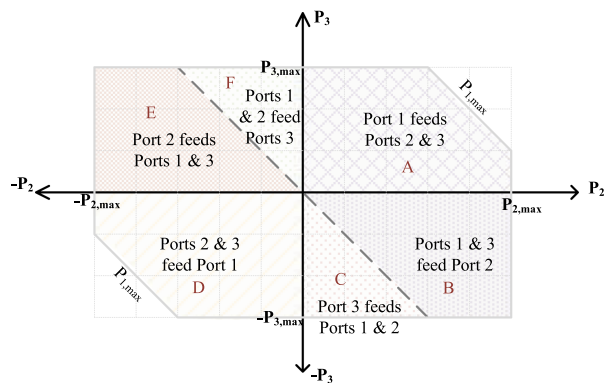t have a resonant tank. The le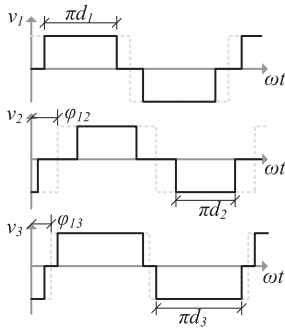akage inductances of the other two ports (ports 1 and 2) are included in the resonant inductances of the respective ports. Hence, they are not shown in Fig. 1. A detailed analysis of the RTPC topology is presented in Section III.

B. MODES OF OPERATION

The modes of operation can be defined based on the direction of power flow among the three ports. The power delivered by port 1 is represented by P_1 and powers received at ports 2 and 3 are represented by P_2 and P_3, respectively. The port 1 power is distributed between ports 2 and 3; $P_1 = P_2 + P_3$. Different modes of operation can be illustrated from the regions in Fig. 2. Mode *A* represents port 1 feeding power to ports 2 and 3; hence, $P_2 > 0$ and $P_3 > 0$. In modes *B*, *C*, and *D*, $P_3 < 0$; hence, port 3 feeds power. Similarly, in modes *D*, *E*, and *F*, port 2 feeds power. The boundary between modes *B* and *C*, and *E* and *F* is $P_3 = -P_2$. When both P_2 and P_3 are negative in mode *D*, ports 2 and 3 feed power to port 1. However, the power flow to/from each port is limited by their respective maximum power rating.

C. PHASE-SHIFT AND DUTY RATIO CONTROL

The conventional two-port resonant converters use frequency modulation (FM) as the control methodology, which enables soft switching [ZVS and zero-current switching (ZCS)]. However, to apply the FM control to an isolated three-port RTPC, at least two of the three ports will need to operate at different switching frequencies. This requires complex mathematical analysis. Therefore, most research on the RTPC concentrates on phase-shift control at constant switching frequency to control the voltage and power flow among the three ports [4], [14], [17], [18]. The control scheme presented here for the proposed topology uses phase-shift and duty ratio control to maximize the efficiency of the converter. Fig. 3 shows the definitions of the five control variables (i.e., ϕ_{12}, ϕ_{13}, d_1, d_2, and d_3) with respect to quasi-square voltage waveforms. The phase shifts of ports 2 and 3 voltages with respect to that of port 1 are defined as ϕ_{12} and ϕ_{13}, respectively, such that $-\pi/2 < \phi_{12}, \phi_{13} < \pi/2$. The duty ratios of the voltage waveforms of ports 1, 2, and 3 are defined as d_1, d_2, and d_3, respectively, such that

FIGURE 3. Definition of control variables with respect to quasi-square waveforms of the RTPC.

FIGURE 4. Equivalent circuit representation of the three-port resonant converter topology. (a) Equivalent circuit. (b) Equivalent delta network.

$0 < d_1, d_2, d_3 < 1$. In Fig. 3, voltages of ports 2 and 3 are lagging port 1 voltage; hence, the two phase-shift values are positive for the mode of operation represented by region A in Fig. 2, where port 1 is feeding ports 2 and 3.

Following the steady-state analysis based on power flow equations presented in Section III and control design in Section IV, it will be evident that the two phase-shift variables are independent control variables and the three duty ratios are dependent control variables. The duty ratios can be defined as functions of the operating point parameters and phase-shift values. To ensure the operation in the inductive region of the resonant converter and realize the ZVS operation for the power feeding port(s) [19], the switching frequency is selected above the resonant frequency, i.e., $F = f_s/f_r > 1$ [14].

The control objective is to control the power transferred to/from two of the three ports so that power transferred to/from the remaining port will be controlled automatically. The development of the control strategy to achieve this objective is presented in Section IV.

III. STEADY-STATE ANALYSIS

Steady-state equations were used to model the RTPC analytically. This allows the accurate modeling of the RTPC, which aids in the verification of the converter operation at different operating conditions.
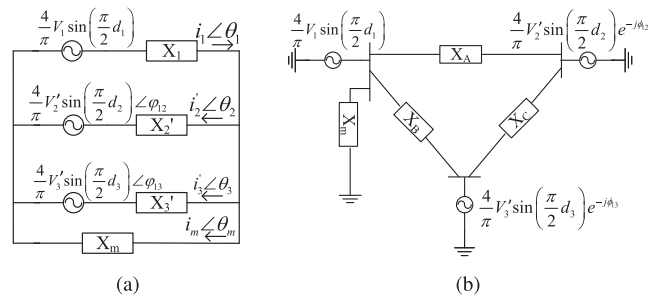
A. POWER FLOW EQUATIONS

The equivalent circuit of the RTPC is shown in Fig. 4(a) with all port voltages, currents, and impedances being referred to port 1. The relationship between V_2', V_3', i_2', i_3', X_2', and X_3' and the turns n_1, n_2, and n_3 at each port is presented as follows:

$$V_2' = V_2 \frac{n_1}{n_2} \tag{1}$$

$$V_3' = V_3 \frac{n_1}{n_3} \tag{2}$$

$$i_2' = i_2 \frac{n_2}{n_1} \tag{3}$$

$$i_3' = i_3 \frac{n_3}{n_1} \tag{4}$$

$$X_2' = X_2 \frac{n_1^2}{n_2^2} \tag{5}$$

$$X_3' = X_3 \frac{n_1^2}{n_3^2}. \tag{6}$$

The fundamental component of the port voltages is represented in polar form, which is a function of the dc-link voltage and the duty ratio of that particular port. This circuit can be transformed to a Delta network, as shown in Fig. 4(b). The impedances X_A, X_B, and X_C represent the equivalent mutual inductances between various ports, and X_D represents the effective self-inductance referred to port 1 predominantly due to the transformer magnetizing inductance. The values of these impedances can be calculated as follows [20]:

$$X_A = X_1 X_2' X \tag{7}$$

$$X_B = X_1 X_3' X \tag{8}$$

$$X_C = X_2' X_3' X \tag{9}$$

$$X_D = X_1 + X_m \tag{10}$$

where X_m is the transformer magnetizing reactance, which is equal to $2\pi f_s L_m$. The reactance X can be calculated as

$$X = \frac{1}{X_1} + \frac{1}{X_2'} + \frac{1}{X_3'} + \frac{1}{X_m}. \tag{11}$$

The steady-state power flow equations between any pair of ports can be derived as a function of the control variables and obtained as

$$P_{12} = \frac{8}{\pi^2} \frac{n_1}{n_2} \frac{V_1 V_2}{X_A} \sin\left(\frac{\pi}{2} d_1\right) \sin\left(\frac{\pi}{2} d_2\right) \sin(\phi_{12}) \tag{12}$$

$$P_{13} = \frac{8}{\pi^2} \frac{n_1}{n_3} \frac{V_1 V_3}{X_B} \sin\left(\frac{\pi}{2} d_1\right) \sin\left(\frac{\pi}{2} d_3\right) \sin(\phi_{13}) \tag{13}$$

$$P_{23} = \frac{8}{\pi^2} \frac{n_1^2}{n_2 n_3} \frac{V_2 V_3}{X_C} \sin\left(\frac{\pi}{2} d_2\right) \sin\left(\frac{\pi}{2} d_3\right) \sin(\phi_{13} - \phi_{12}). \tag{14}$$

Power received/delivered at each port can be calculated using (15)–(17). For zero circulating currents among the three

ports, (18) needs to be satisfied

$$P_1 = P_{12} + P_{13} \qquad (15)$$

$$P_2 = P_{12} - P_{23} \qquad (16)$$

$$P_3 = P_{13} + P_{23} \qquad (17)$$

$$P_{12} + P_{23} = P_{13}. \qquad (18)$$

The power flow between the ports can be controlled by varying the phase-shift angles between the corresponding port voltages, adjusting the duty ratio, or a combination of both, which provides a higher degree of freedom for the converter control.

1) RESONANT TANK PARAMETERS

For the converter to operate over a wide voltage and power range, at various operating conditions, the accurate selection of resonant tank parameters (i.e., resonant tank component values) is critical. Therefore, a set of criteria can be used to determine the values for the resonant tank components: L_1, L_2, C_1, C_2, and L_m based on Fig. 1.

The ratio between the resonant tank parameters are defined as $h = L_m/L_1$, $k = L_2/L_1$, and $g = C_2/C_1$. The resonant frequency can be defined in terms of resonant tank elements, as seen from (19). Since both the resonant tanks share the same resonant frequency, a relationship between k and g can be derived based on (20). Hence, port 2 resonant tank elements can be defined as a function of k, g, and port 1 resonant tank elements obtained from (21)

$$f_r = \frac{1}{2\pi\sqrt{L_1 C_1}}, f_r = \frac{1}{2\pi\sqrt{L_2 C_2}} \qquad (19)$$

$$kg = 1 \qquad (20)$$

$$C_2 = gC_1, L_2 = L_1/g. \qquad (21)$$

The converter impedance can be derived as a function of F, f_s, C_1, g, h, and L_{lk3} according to (22)–(25). These can be used to derive the impedances X_A, X_B, and X_C of the equivalent delta network using (7)–(11)

$$X_1 = \frac{F^2 - 1}{2\pi f_s C_1} \qquad (22)$$

$$X_2 = \frac{F^2 - 1}{2\pi f_s g C_1} = \frac{X_1}{g} \qquad (23)$$

$$X_3 = 2\pi f_s L_{lk3} \qquad (24)$$

$$X_m = 2\pi f_s h L_1 = \frac{hF^2 X_1}{F^2 - 1}. \qquad (25)$$

The magnetizing inductance should be sufficiently higher than the resonant inductance to minimize the circulating currents. It is recommended to maintain the ratio between the magnetizing and resonant inductance greater than $h_{\min}$. In this article, $h_{\min} = 4$. Hence, the first condition can be derived

with reference to L_1 and L_2 based on

$$h > h_{\min}, \qquad hg > h_{\min}\frac{n_1^2}{n_2^2} \rightarrow \text{condition 1.} \qquad (26)$$

For $-\pi/2 < \phi_{12} < \pi/2$, $-\pi/2 < \phi_{13} < \pi/2$, and $0 < d_1, d_2, d_3 < 1$, the remaining conditions can be derived based on the formulas for P_{12}, P_{13}, and P_{23} from (12)–(14). $P_{12,\max}$, $P_{13,\max}$, and $P_{23,\max}$ can be calculated based on $P_{1,\max}$, $P_{2,\max}$, and $P_{3,\max}$ using (15)–(18)

$$\frac{\pi^2}{8}\frac{n_2}{n_1}\frac{X_A}{V_{1,\min}V_{2,\min}}P_{12,\max} < 1 \rightarrow \text{condition 2} \qquad (27)$$

$$\frac{\pi^2}{8}\frac{n_3}{n_1}\frac{X_B}{V_{1,\min}V_{3,\min}}P_{13,\max} < 1 \rightarrow \text{condition 3} \qquad (28)$$

$$\frac{\pi^2}{8}\frac{n_2 n_3}{n_1^2}\frac{X_C}{V_{2,\min}V_{3,\min}}P_{23,\max} < 1 \rightarrow \text{condition 4.} \qquad (29)$$

Applying (22)–(25) in (27)–(29), conditions 2, 3, and 4 can be expressed in terms of F, f_s, C_1, g, h, and L_{lk3}. First, f_s can be fixed based on the switching device capabilities. Lower the resonant frequency, higher will be values of resonant inductor and capacitor, as indicated in (19). Therefore, the ratio (F) between switching and resonant frequency can be selected closer to 1 to limit the size of the resonant tank while ensuring resonant tank operation in the inductive region. In this article, $F = 1.1$.

The parameter L_{lk3} can be selected based on the type of three-winding transformer used (i.e., regular switched mode power supply, transformer, or planar transformer). The turns ratio ($n_1 : n_2 : n_3$) can be set based on the nominal voltages of the three ports. The remaining unknowns in the above analysis, C_1, h, and g, can be estimated to satisfy the four conditions computed from (26)–(29). Limiting the value/size of C_2 is also considered when setting a value for g. Once the values for C_1, h, and g are set, the remaining resonant tank parameters can be evaluated.

It is important to verify the above conditions under ±5% to ±10% variation, for the resonant tank parameters to ensure effective converter operation over the entire operating range. The value obtained for the magnetizing inductance (L_m) can be considered as the minimum required value during the transformer design process (i.e., $L_m \geq hL_1$). Port 3 leakage inductance (L_{lk3}) may impact the power flow and resonant tank parameter calculation. Following the initial design process, the above conditions can be validated for the measured L_{lk3} of the three-winding transformer. When designing the converter magnetics, the compensation of a portion of resonant inductance from the transformer leakage inductance must to be considered.

2) DC-LINK CAPACITORS

The dc-link capacitors on all three ports play a crucial role in maintaining a low ripple dc voltage for correct converter operation. By providing a low impedance path at higher frequencies, the capacitors also filter high-frequency ac current

ripples generated by the HV battery on port 1 and the full-bridges on ports 2 and 3 [21]. Therefore, the accurate design of the dc-link capacitors (C_{P1}, C_{P2}, and C_{P3}) becomes necessary.

The analysis can be done in terms of phasors based on the equivalent circuit in Fig. 4(a), in which $i_1 \underline{/\theta_1}$, $i_2' \underline{/\vartheta_2}$, $i_3' \underline{/\vartheta_3}$, and $i_m \underline{/\vartheta_m}$ denote the current through X_1, X_2, X_3, and X_m and their associated phase angles, respectively. For simplicity, the analysis is completed under the assumption of operating mode A, in which port 1 supplies power to ports 2 and 3. Hence, an equation for the currents seen in Fig. 4(a) is obtained as

$$i_1 \underline{/\vartheta_1} = i_2' \underline{/\vartheta_2} + i_3' \underline{/\vartheta_3} + i_m \underline{/\vartheta_m}. \tag{30}$$

Since ports 2 and 3 are being referred to the port 1 side, $V_p \angle \alpha$ is the voltage across the primary winding of the transformer, with phase angle α. Owing to the voltage drop across X_1, X_2, X_3, and X_m, (31)–(34) are obtained with the port 1 phase angle, ϕ_1, set to zero. The phase angles of port 2 and port 3 voltages are denoted by ϕ_{12} and ϕ_{13}, respectively

$$\frac{4}{\pi} V_1 \sin\left(\frac{\pi}{2} d_1\right) \underline{/0} - V_p \underline{/\alpha} = X_1 i_1 \underline{/\vartheta_1 + \frac{\pi}{2}} \tag{31}$$

$$V_p \underline{/\alpha} - \frac{4}{\pi} \frac{n_1}{n_2} V_2 \sin\left(\frac{\pi}{2} d_2\right) \underline{/\varphi_{12}} = \frac{n_1^2}{n_2^2} X_2 i_2' \underline{/\vartheta_2 + \frac{\pi}{2}} \tag{32}$$

$$V_p \underline{/\alpha} - \frac{4}{\pi} \frac{n_1}{n_3} V_3 \sin\left(\frac{\pi}{2} d_3\right) \underline{/\varphi_{13}} = \frac{n_1^2}{n_3^2} X_3 i_3' \underline{/\vartheta_3 + \frac{\pi}{2}} \tag{33}$$

$$V_p \underline{/\alpha} = X_m i_m \underline{/\vartheta_m + \frac{\pi}{2}}. \tag{34}$$

Calculating the necessary dc-link capacitance at all three ports requires i_1, i_2, i_3, i_m, and V_p. Hence, (30)–(34) can be used to solve for the unknown variables, assuming that V_1, V_2, V_3, n_1, n_2, n_3, X_1, X_2, and X_3 are determined and d_1, d_2, d_3, ϕ_{12}, and ϕ_{13} are chosen to operate in a specific operating region, as presented in Section IV. The unknown variables can be decomposed into sine and cosine components and solved using a numerical solver to obtain i_1, i_2, and i_3, representing the peak currents of the three ports. Peak currents, $i_{\text{peak},1}$, $i_{\text{peak},2}$, and $i_{\text{peak},3}$, are shown in (35)–(37), where $i_{n,\sin}$ and $i_{n,\cos}$ are the sine and cosine components and n represents the port number

$$i_{\text{peak},1} = \sqrt{i_{1,\sin}^2 + i_{1,\cos}^2} \tag{35}$$

$$i_{\text{peak},2} = \frac{n_1}{n_2} \sqrt{i_{2,\sin}^2 + i_{2,\cos}^2} \tag{36}$$

$$i_{\text{peak},3} = \frac{n_1}{n_3} \sqrt{i_{3,\sin}^2 + i_{3,\cos}^2}. \tag{37}$$

Assuming a dc current of $I_{\text{dc},n}$ at ports $n = 1, 2, 3$, the root-mean-square (RMS) current through each dc-link capacitor at port n ($i_{C_{Pn},\text{RMS}}$) can be calculated from (38), since the ac currents are assumed to be purely sinusoidal

$$i_{C_{Pn},\text{RMS}} = \frac{1}{\sqrt{2}} \left(i_{\text{peak},n} - I_{\text{dc},n}\right). \tag{38}$$

Based on the capacitor charge relationship, $C = \frac{Q}{V}$, the dc-link capacitance for port n (C_{Pn}) is obtained from (39), where

TABLE 1. Comparison of Analytical and Simulation Results

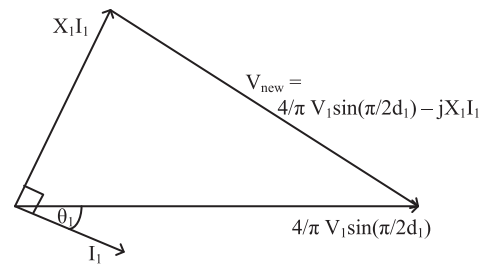| Operating Point	Port	Simulated i_{peak} (A)	Analytical i_{peak} (A)	Error (%)
$OP1$	1	25.7	26.6	4
$OP1$	2	161.3	155.8	3
$OP1$	3	686.9	652.1	5
$OP2$	1	24.7	22.7	8
$OP2$	2	137.8	130.6	5
$OP2$	3	612.7	631.2	3

FIGURE 5. Phasor diagram for port 1.

ΔV is the peak-to-peak voltage ripple. The ripple period is defined as $\Delta t = \frac{1}{2 f_s}$

$$C_{Pn} = i_{C_{Pn},\text{RMS}} \frac{1}{2 f_s} \frac{1}{\Delta V}. \tag{39}$$

A comparison between the analytical results obtained from (35)–(37) and PLECS simulation results is shown in Table 1. Assuming a wide operating voltage on all three ports, operating points 1 and 2, denoted as $OP1$ and $OP2$ respectively, refer to two worst-case voltage combinations on the three ports. $OP1$ and $OP2$ represent the operating points where $V_1 = 400$ V, $V_2 = 48$ V, $V_3 = 12$ V and $V_1 = 800$ V, $V_2 = 48$ V, $V_3 = 12$ V, respectively. The maximum error of 8%, 5%, and 5% is obtained for $i_{\text{peak},1}$, $i_{\text{peak},2}$, and $i_{\text{peak},3}$, respectively. The accuracy of the derived equations for designing the dc-link capacitors of the RTPC is, therefore, validated. To calculate the dc-link capacitance and ensure that it is sufficient for the worst-case operating points, a 20% margin must be considered for each port, based on the maximum RMS current.

B. SOFT-SWITCHING BOUNDARY CONDITIONS

Resonant converters inherit ZVS and ZCS with variable frequency control [22], [23], [24]. However, with phase-shift and duty ratio control for the RTPC, the ZVS region is limited, because the impedance of the resonant tank remains constant at a fixed switching frequency. To achieve ZVS, the current should be lagging the voltage for the power feeding port(s), and the current should be leading the voltage for the power receiving port(s). The ZVS boundaries for the three ports for different modes of operation are derived from the phasor analysis and are summarized below.

For operating mode A, port 1 feeds ports 2 and 3, and port 1 voltage should lead the current, as shown in Fig. 5, to achieve ZVS. The condition to achieve ZVS can be derived based on the inequality given in (40). Simplifying this condition will

show that port 1 will have ZVS for the entire voltage and load range at operating mode A. Similarly, ZVS conditions for ports 2 and 3 can be derived for the respective currents to lead the voltages using phasor diagram analysis. The conditions for ports 2 and 3 can be simplified as (41) and (42), respectively. With the soft switching boundary conditions established, the concerns of transformer coil misalignment affecting soft switching are addressed, as outlined in [25]

$$V_{\text{new}}^2 < \left[\frac{4}{\pi}V_1\sin\left(\frac{\pi}{2}d_1\right)\right]^2 + [X_1 I_1]^2 \tag{40}$$

$$\frac{1}{h}\left(1 - \frac{1}{F_1^2}\right) > \frac{V_1}{V_2}\frac{n_2}{n_1} - 1 \tag{41}$$

$$\frac{1}{h}\left(1 - \frac{1}{F_1^2}\right) > \frac{V_1}{V_3}\frac{n_3}{n_1} - 1. \tag{42}$$

With reference to these derived conditions, ZVS boundaries for operating mode A can be obtained as follows: port 1 will have ZVS for the entire operating range; ports 2 and 3 will achieve ZVS when $V_1 < V_{1,\text{nominal}}$, i.e., buck operation. Similarly, ZVS boundaries for the other modes of operation can be obtained.

For operating mode E, where port 2 feeds ports 1 and 3, ZVS boundaries are similar to those of mode A. For operating mode F, where ports 1 and 2 feed port 3, port 1 will achieve ZVS for $V_1 > V_{1,\text{nominal}}$, i.e., boost operation, and ports 2 and 3 will achieve ZVS for buck operation.

IV. CONTROL DESIGN
To regulate the port voltages, a closed-loop control system is required. Since the converter operates bidirectionally, it is crucial to design a robust controller that can handle different power flow configurations. As discussed in Section II, the closed-loop control can be developed for two of the three ports so that the power flow to/from the remaining port is automatically controlled. There are two current loops for ports 2 and 3 to evaluate the control variables at each operating point. The developed controller will sense the currents of ports 2 and 3, with port 2 voltage. A nested control loop strategy is employed for port 2, with the outer voltage loop providing the reference current for port 2. Since the duty ratio can be derived as a function of phase shift for a given operating point, the two current control loops will control the relevant phase-shift angles.

A. STATE-SPACE EQUATIONS
State-space equations are derived to model the dynamic behavior of the three-port resonant converter analytically. In contrast to conventional switched-mode power supplies, small-signal approximation cannot be applied in the case of a resonant converter because of the large variation in port voltage and current waveforms. Hence, a generalized state-space averaging technique is used to derive the dynamic equations of the converter under the assumption that only the fundamental

components of voltage and current contribute to the power flow between various ports [26]. The nonidealities of the converter semiconductor switches are neglected in the derivation of the state-space equations. The state equations of the TPC can be obtained from the following equations:

$$L_1\frac{di_1}{dt} = V_1\text{sgn}\{\sin(\omega t)\} - v_{c1}$$
$$- \frac{n_1}{n_3}V_3\text{sgn}\{\sin(\omega t - \Phi_{13})\} \tag{43}$$

$$C_1\frac{dv_{c1}}{dt} = i_1 \tag{44}$$

$$L_2\frac{di_2}{dt} = \frac{n_2}{n_3}V_3\text{sgn}\{\sin(\omega t - \Phi_{13})\} - v_{c2}$$
$$- v_2\text{sgn}\{\sin(\omega t - \Phi_{12})\} \tag{45}$$

$$C_2\frac{dv_{c2}}{dt} = i_2 \tag{46}$$

$$C_{P2}\frac{dv_2}{dt} = i_2\text{sgn}\{\sin(\omega t - \Phi_{12})\} - \frac{v_2}{R_2}. \tag{47}$$

The sgn(.) operator is used to take into account the polarity of the tank input voltage in the state equations. The tank voltage and tank current equations can be represented in the polar form using the techniques provided in [26] as follows:

$$\frac{di_1}{dt} = -j\omega_s i_1 - j\frac{2}{\pi L_1}V_1 - \frac{v_{c1}}{L_1} + j\frac{2}{\pi L_1}\frac{n_1}{n_3}V_3 e^{-j\Phi_{13}} \tag{48}$$

$$\frac{dv_{c1}}{dt} = -j\omega_s v_{c1} + \frac{i_1}{C_1} \tag{49}$$

$$\frac{di_2}{dt} = -j\omega_s i_2 - j\frac{n_2}{n_3}\frac{2}{\pi L_2}V_3 e^{-j\Phi_{13}} - \frac{v_{c2}}{L_2} + j\frac{2}{\pi L_2}v_2 e^{-j\Phi_{12}} \tag{50}$$

$$\frac{dv_{c2}}{dt} = -j\omega_s v_{c2} + \frac{i_2}{C_2} \tag{51}$$

$$\frac{dv_2}{dt} = -j\frac{2}{\pi C_{P2}}i_2 e^{-j\Phi_{12}} + j\frac{2}{\pi C_{P2}}i_2 e^{j\Phi_{12}} - \frac{v_2}{R_2 C_{P2}}. \tag{52}$$

The final state equations are derived by extracting the real and imaginary components of the converter state equations, where tank voltage and current waveforms are represented in the rectangular form according to the following equation:

$$\begin{cases} i_1 = x_1 + jx_2 \\ v_{c1} = x_3 + jx_4 \\ i_2 = x_5 + jx_6 \\ v_{c2} = x_7 + jx_8. \end{cases} \tag{53}$$

The final state equations are represented in (54)–(62), where the steady-state values of the tank voltages and tank currents
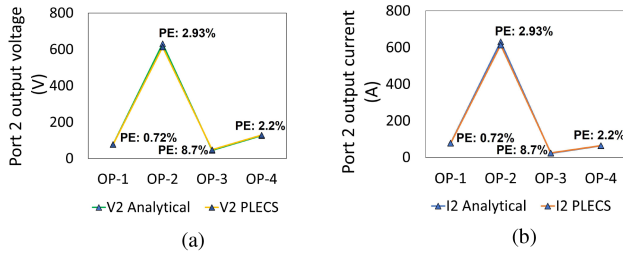
FIGURE 6. Comparison of the analytical results obtained from the state-space analysis, with simulation results from PLECS, in terms of percentage error (PE). (a) Port 2 voltage. (b) Port 2 current.

are calculated by equating the derivative term to zero

$$x_1 = \frac{2}{\pi Z_1}\left(\frac{F}{F^2-1}\right)\left\{\frac{n_1}{n_3}V_3\cos(\Phi_{13}) - V_1\right\} \quad (54)$$

$$x_2 = \frac{2n_1}{n_3\pi Z_1}\left(\frac{F}{F^2-1}\right)V_3\sin(\Phi_{13}) \quad (55)$$

$$x_3 = \frac{Z_1}{F}x_2 \quad (56)$$

$$x_4 = \frac{-Z_1}{F}x_1 \quad (57)$$

$$x_5 = \frac{2}{\pi Z_2}\left(\frac{F}{F^2-1}\right)\left\{x_9\cos(\Phi_{12}) - \frac{n_2}{n_3}V_3\cos(\Phi_{13})\right\} \quad (58)$$

$$x_6 = \frac{2}{\pi Z_2}\left(\frac{F}{F^2-1}\right)\left\{-x_9\sin(\Phi_{12}) + \frac{n_2}{n_3}V_3\sin(\Phi_{13})\right\} \quad (59)$$

$$x_7 = \frac{Z_2}{F}x_6 \quad (60)$$

$$x_8 = \frac{-Z_2}{F}x_5 \quad (61)$$

where $Z_i = \sqrt{\frac{L_i}{C_i}}$, for $i = 1, 2$. The output voltage v_2 can be obtained as

$$v_2 = \frac{8}{\pi^2}R_2\left\{\frac{n_3}{n_2}V_3\left(\frac{F}{Z_2(1-F^2)}\right)\sin(\Phi_{12} - \Phi_{13})\right.$$
$$\left. - \frac{n_1}{n_2}V_1\left(\frac{F}{Z_1(1-F^2)}\right)\sin(\Phi_{12})\right\}. \quad (62)$$

The state-space equations were validated against the PLECS simulation results, at four operating points, as demonstrated in Fig. 6. Operating point 1 (OP-1) represents the case where $\Phi_{12} = 3.6°$ and $\Phi_{13} = 7.2°$ and operating point 2 is for $\Phi_{12} = 32.4°$ and $\Phi_{13} = 28.8°$. Operating points 3 and 4 are corresponding to $\Phi_{12} = \Phi_{13} = 1.1°$ and $\Phi_{12} = 3.24°$, $\Phi_{13} = -0.72°$, respectively. As seen from Fig. 6, the results obtained from the derived formulas match closely with the simulation results, validating the accuracy of the derived formulas used to model the converter analytically ($PE < 9\%$). Equation (62) represents the average output voltage at port 2 as a function of the phase-shift angle between various ports. The port 2 output voltage also depends on the port 2 load resistor (R_2), tank parameters, transformer turns ratio, and port 1 and 3 voltages.
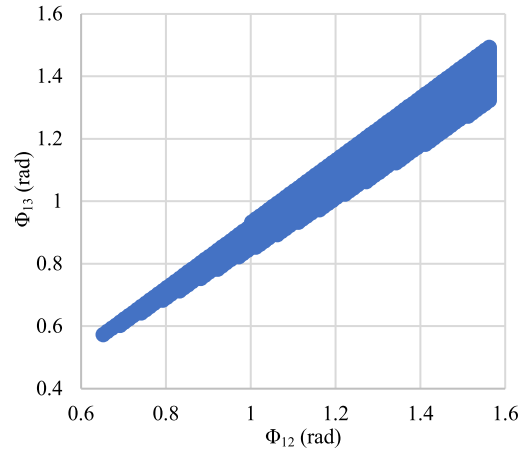
FIGURE 7. Admissible range of phase shift for the operating point of $V_1 = 600$ V, $V_2 = 48$ V, and $V_3 = 12$ V with $P_1 = 6$ kW, $P_2 = 3.18$ kW, and $P_3 = P_1 - P_2$ in the designed prototype.

Since port 2 power is independent of the load resistor, port 2 voltage can be regulated via phase-shift control based on (62).

B. EVALUATING THE OPTIMUM CONTROL POINT

The duty ratio values at each operating point can be calculated using the following equations, which are derived from the power flow equations presented in Section III:

$$d_1 = \frac{2}{\pi}\sin^{-1}\sqrt{\frac{\pi^2}{8}\frac{X_AX_B}{X_C}\frac{1}{V_1^2}\frac{P_{12}P_{13}}{P_{23}}\frac{\sin(\phi_{13}-\phi_{12})}{\sin\phi_{12}\sin\phi_{13}}} \quad (63)$$

$$d_2 = \frac{2}{\pi}\sin^{-1}\sqrt{\frac{\pi^2}{8}\frac{n_2}{n_1}\frac{X_A}{V_1V_2}\frac{P_{12}}{\sin\phi_{12}\sin\left(\frac{\pi}{2}d_1\right)}} \quad (64)$$

$$d_3 = \frac{2}{\pi}\sin^{-1}\sqrt{\frac{\pi^2}{8}\frac{n_3}{n_1}\frac{X_B}{V_1V_3}\frac{P_{13}}{\sin\phi_{13}\sin\left(\frac{\pi}{2}d_1\right)}}. \quad (65)$$

From the power flow equations, it can be observed that for a single operating point (i.e., fixed power level at the three ports), there exist multiple combinations of phase-shift and duty ratio values that the converter can operate at. Fig. 7 shows the admissible range of phase shift for the RTPC to operate at a single operating point. At each pair of phase shift within the admissible range, there exists a definite combination of duty ratio. This admissible range is obtained through constraints on control variables such as $0 < d_1, d_2, d_3 < 1$, $\phi_{12} > \phi_{13}$ for $P_2 > P_3$ and $\phi_{12} < \phi_{13}$ for $P_2 < P_3$.

From the admissible range, the optimum control point can be determined to operate the converter with minimum loss. In this article, the optimum control point is identified by running a series of open-loop simulations on the RTPC model to evaluate the efficiency within the admissible range. Since there are two control loops to control the independent control variables ϕ_{12} and ϕ_{13}, the dependent duty ratio values for the optimum control point can be stored in lookup tables (LUTs). The LUTs are based on the reference voltage and current of the three ports.

C. DECOUPLING NETWORK

Power flow analysis presented in Section II shows that the power flow to each port is a function of phase-shift variables ϕ_{12} and ϕ_{13}. As a result, power flow to any port cannot be controlled independently using only one of the phase-shift angles. This dependence can be recognized as a coupling between the two phase shifts. Hence, to control each port's power flow independently, a decoupling network is required. There are two types of decoupling: hardware decoupling and soft or control decoupling. Hardware decoupling is presented in [14] and [15]. In hardware decoupling, only one mode of operation is considered, and resonant components are selected to manage the impedances to maximize the power flow in one direction and minimize it in other directions. When different modes of operation are considered, a soft or control decoupling network can be used. A control decoupling network for a TAB was presented in [21]. This work follows a similar approach to develop a decoupling network for an RTPC.

The decoupling network derivation presented below considers operating mode A, where power flows from port 1 to ports 2 and 3. However, the same network can also be used for other modes of operation. Currents received at ports 2 and 3 (I_2 and I_3, respectively) can be equated as (66) and (67) based on the power flow equations presented in (12)–(17)

$$I_2 = \frac{8}{\pi^2} \frac{n_1}{n_2} \frac{V_1}{X_A} \sin\left(\frac{\pi}{2}d_1\right) \sin\left(\frac{\pi}{2}d_2\right) \sin(\phi_{12})$$
$$- \frac{8}{\pi^2} \frac{n_1^2}{n_2 n_3} \frac{V_3}{X_C} \sin\left(\frac{\pi}{2}d_2\right) \sin\left(\frac{\pi}{2}d_3\right) \sin(\phi_{13} - \phi_{12})$$
$$(66)$$

$$I_3 = \frac{8}{\pi^2} \frac{n_1}{n_3} \frac{V_1}{X_B} \sin\left(\frac{\pi}{2}d_1\right) \sin\left(\frac{\pi}{2}d_3\right) \sin(\phi_{13})$$
$$+ \frac{8}{\pi^2} \frac{n_1^2}{n_2 n_3} \frac{V_2}{X_C} \sin\left(\frac{\pi}{2}d_2\right) \sin\left(\frac{\pi}{2}d_3\right) \sin(\phi_{13} - \phi_{12}).$$
$$(67)$$

Taylor series expansion for two variables can be applied to (66) and (67) at an operating point (Φ_{12}, Φ_{13}) such that $\phi_{12} = \Phi_{12} + \Delta\phi_{12}$, $\phi_{13} = \Phi_{13} + \Delta\phi_{13}$, $I_2 = \mathbf{I_2} + \Delta I_2$, and $I_3 = \mathbf{I_3} + \Delta I_3$ [27]. This will result in (68), where G is the coupling matrix. The elements G_{12} and G_{21} of the coupling matrix G create the interaction between the two current loops

$$\Delta I = \begin{bmatrix} \Delta I_2 \\ \Delta I_3 \end{bmatrix} = \begin{bmatrix} G_{11} & G_{12} \\ G_{21} & G_{22} \end{bmatrix} \begin{bmatrix} \Delta\phi_{12} \\ \Delta\phi_{13} \end{bmatrix} = G\Delta\phi \quad (68)$$

$$G_{11} = \frac{8}{\pi^2} \frac{n_1}{n_2} \frac{V_1}{X_A} \sin\left(\frac{\pi}{2}d_1\right) \sin\left(\frac{\pi}{2}d_2\right) \cos(\Phi_{12})$$
$$+ \frac{8}{\pi^2} \frac{n_1^2}{n_2 n_3} \frac{V_3}{X_C} \sin\left(\frac{\pi}{2}d_2\right) \sin\left(\frac{\pi}{2}d_3\right) \cos(\Phi_{13} - \Phi_{12})$$
$$(69)$$

$$G_{12} = -\frac{8}{\pi^2} \frac{n_1^2}{n_2 n_3} \frac{V_3}{X_C}$$

$$\sin\left(\frac{\pi}{2}d_2\right) \sin\left(\frac{\pi}{2}d_3\right) \cos(\Phi_{13} - \Phi_{12}) \quad (70)$$

$$G_{21} = -\frac{8}{\pi^2} \frac{n_1^2}{n_2 n_3} \frac{V_2}{X_C}$$

$$\sin\left(\frac{\pi}{2}d_2\right) \sin\left(\frac{\pi}{2}d_3\right) \cos(\Phi_{13} - \Phi_{12}) \quad (71)$$

$$G_{22} = \frac{8}{\pi^2} \frac{n_1}{n_3} \frac{V_1}{X_B} \sin\left(\frac{\pi}{2}d_1\right) \sin\left(\frac{\pi}{2}d_3\right) \cos(\Phi_{13})$$
$$+ \frac{8}{\pi^2} \frac{n_1^2}{n_2 n_3} \frac{V_2}{X_C} \sin\left(\frac{\pi}{2}d_2\right) \sin\left(\frac{\pi}{2}d_3\right) \cos(\Phi_{13} - \Phi_{12}).$$
$$(72)$$

The coupling between the two current loops can be cancelled through multiplication by the inverse of the coupling matrix G. Hence, the decoupling matrix can be defined as (73) such that $HG = I$. This will create independent control loops for I_2 and I_3

$$H = G^{-1}. \quad (73)$$

It can be observed that the elements of the decoupling matrix are a function of the five control variables and voltages of the three ports. Therefore, these elements should be calculated at each operating point with reference to the relevant control variable values. In [21], the elements of the decoupling matrix are calculated offline at the optimum control point for each operating point and stored in an LUT for the closed-loop control. In this article, parameters of the decoupling matrix are calculated online with the real-time calculation of the phase-shift angles, optimum duty ratios obtained from LUTs, and with consideration of the three port voltages.

D. CLOSED-LOOP CONTROL STRATEGY

The proposed controller is presented in Fig. 8. At first, the measured port 2 voltage and port 3 current are compared to their reference values. Port 3 reference current is provided to the controller as an input, assuming a battery at the port 3 output, which is the case in an EV. Port 2 has an outer voltage loop and an inner current loop. The current compensators of ports 2 and 3 generate the decoupled phase-shift angles between ports 1 and 2, referred to as ϕ'_{12} and that between ports 1 and 3, referred to as ϕ'_{13}. The decoupled phase-shift angles ϕ'_{12} and ϕ'_{13} are passed onto the decoupling matrix, derived in the previous section.

The voltage and current at a specific operating point is passed onto the LUTs for optimum duty ratio calculation. As previously discussed, a combinational phase-shift and duty ratio controller is employed to maximize the efficiency over a wide operating range. The duty cycles for each port are obtained and passed to the RTPC along with the coupled phase-shift angles. The controller then repeats this process to account for any load or input voltage variations. The proposed control strategy can be implemented in an offline manner on any digital signal process such as the Texas Instruments C2000 F28379D Launchpad. It should also be noted that propagation delays in the gate signals of the three ports can add
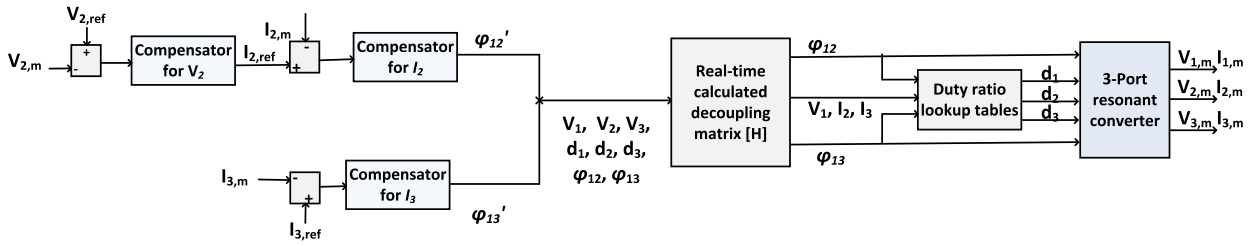
FIGURE 8. Nested closed-loop control strategy.

TABLE 2. Ratings and Parameters of the RTPC

	Port 1	Port 2	Port 3
Voltage Range	400–800 V	46–50 V	10–14 V
Max Power	6 kW	5 kW	3 kW
Turns Ratio		50 : 4 : 1	
Resonant Inductance	87.5 μH	1.8 μH	-
Resonant Capacitance	35 nF	1715 nF	-
Magnetizing Inductance		> 1.1 mH	

additional phase shifts to the system. This can be addressed by the careful selection of the isolated gate drivers with matching propagation delays for the three ports, while considering careful gate driver printed circuit board design with similar gate signal lengths.

V. SIMULATION RESULTS

The specifications of the RTPC are provided in Table 2. The resonant tank parameters calculated based on the method discussed in Section III are also shown.

A. IMPLEMENTATION OF CONTROL STRATEGY

The control strategy based on current and voltage sensing of port 2 and current sensing of port 3 was implemented in the PLECS simulation environment. The controller configuration is presented in Fig. 8.

Initially, the open-loop control is implemented and tested in PLECS. The optimum duty ratio LUTs are implemented in 3-D LUTs to be referenced by using port 1 voltage, port 2 current, and port 3 current. Only the currents in ports 2 and 3 are considered, neglecting the effect of voltage variation in the respective ports. However, the accuracy of the control loop can be improved further by taking into account the voltages of ports 2 and 3 as well.

In order to design the closed-loop current and voltage compensators, the plant bode plot is determined. The plant considered for the bode plot is including the real-time calculation-based decoupling matrix. The plant bode plots for the port 2 and port 3 current response demonstrated in Fig. 9 show that they are type 0 systems, and integral controllers can be used to manage the steady-state error < 2% at a cutoff frequency of 1 kHz. In addition, lead compensators are incorporated to improve the stability of the system and manage a phase margin of 60° [28].
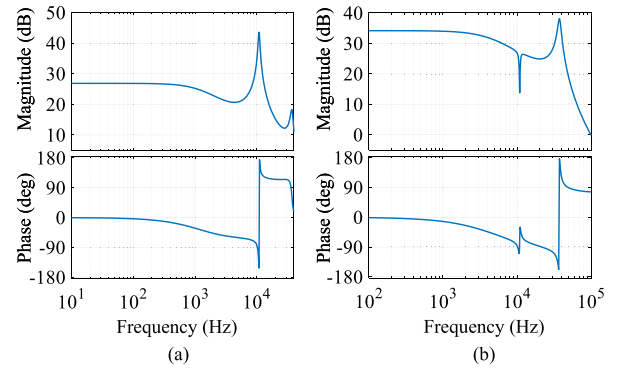

FIGURE 9. Plant bode plots for the current loops of (a) port 2 and (b) port 3 at $V_1 = 600$ V, $P_1 = 6$ kW, $P_2 = 3.18$ kW, and $P_3 = 2.82$ kW.

TABLE 3. Characteristics of the Developed Closed-Loop Control

Control loop	Gain margin	Phase margin	Cut-off frequency
Port 2 outer voltage loop	25.8 dB	68°	100 Hz
Port 2 inner current loop	43.5 dB	60°	1 kHz
Port 3 current loop	21.5 dB	60°	1 kHz

The compensators for $V_2, I_2,$ and I_3 are represented as TF_{V2}, TF_{I2}, and TF_{I3}, respectively. TF_{V2} was designed based on the crossover frequency f_c, where f_c was selected to be less than one-tenth the switching frequency. The pole frequency was selected as a tenth of the crossover frequency. The characteristics of the developed control loops are given in Table 3. The following transfer functions are obtained
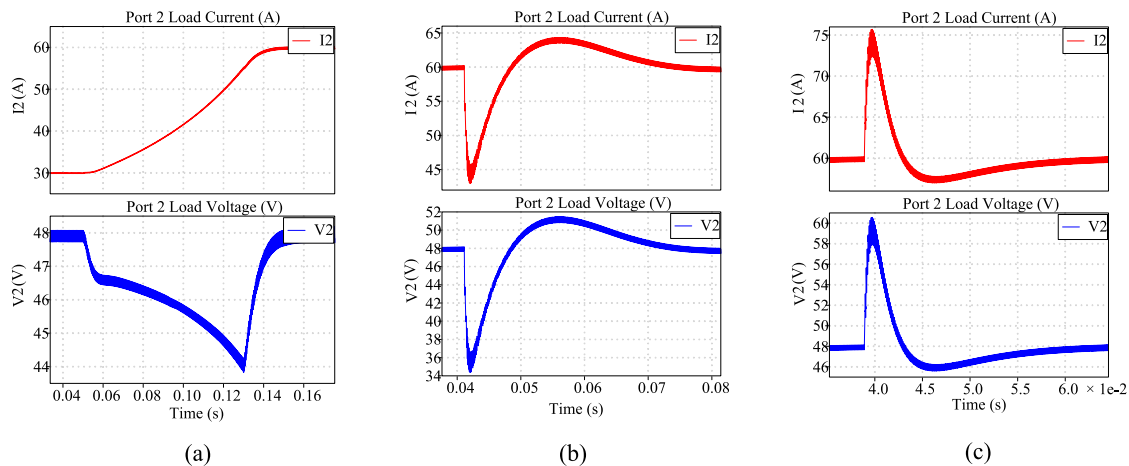
$$TF_{V2} = \frac{0.055s + 157.83}{s} \qquad (74)$$

$$TF_{I2} = 572\frac{s + 5757}{s^2 + 8912s} \qquad (75)$$

$$TF_{I3} = 1150\frac{s + 17287}{s^2 + 26555s}. \qquad (76)$$

B. CLOSED-LOOP DESIGN VALIDATION

In this section, the controller concept presented in Fig. 8 is verified. To verify the controller and ensure that the converter can handle any disturbances, a number of tests can be implemented. Among those, are the step-load and input voltage

FIGURE 10. Closed-loop controller test. (a) Step-load test on port 2; half-load to full-load. (b) Input voltage variation test for change in input voltage from 600 to 400 V. (c) Input voltage variation test for change in input voltage from 600 to 800 V.

TABLE 4. Port 2 Settling Time and Voltage Variation Under Different Tests

Test	Port 2 settling time	Port 2 voltage drop
Step-load test (half-load to full-load) at port 2	92 ms	8%
Input voltage variation from 600 V to 400 V	32 ms	26%
Input voltage variation from 600 V to 800 V	27 ms	24%

variation tests. In the step-load test, the load changes and the output voltage is monitored to ensure regulation and address the concerns of transformer coil misalignment, which could impact output oscillations [25]. The input voltage variation test varies the input voltage and observes whether the converter can maintain its output voltage. The results obtained under each test are presented in this section and are summarized in Table 4.

1) STEP-LOAD TEST

A step-load test where the load is changed from half-load to full-load (full power) at port 2 is conducted in the PLECS environment. The results are shown in Fig. 10(a). Within 92 ms, the port 2 voltage regulates to its nominal (48 V) value, verifying the effectiveness of the proposed controller. The voltage drop is well within an acceptable range (<4 V on the 48-V port), and the results are, therefore, validated.

2) INPUT VOLTAGE VARIATION

Under the input voltage variation test, the voltage on port 1 is modified from the nominal 600 V to the extreme voltages of 400 and 800 V. The impact of this voltage change on the port 2 voltage is observed. The results are shown in Fig. 10(b) and (c). As seen from Fig. 10(b), modifying the voltage from 600 to 400 V leads to 26% voltage drop and the port 2 voltage regulates to its nominal value within 32 ms. According to

Fig. 10(c), with port 1 voltage changing from 600 to 800 V, a 24% voltage drop is observed with a settling time of 27 ms. Thus, the proposed controller is effective at regulating the port 2 voltage under input voltage variation. It is worth mentioning that to further validate the proposed control strategy, thermal analysis is required to ensure that the controller is maintaining converter operation at all operating points. This will be addressed as part of future work.

VI. CONCLUSION

In this article, a control strategy for an isolated bidirectional RTPC was proposed for EV applications. The presented topology maintained converter operation across a wide operating range and at different load conditions. The steady-state analysis of the converter was conducted, outlining the power flow and soft switching conditions of the RTPC. An analytical model of the converter was derived based on state-space equations that can be used to accurately model the converter. A decoupled control strategy was employed to permit independent control of the three ports. A nested control loop strategy based on voltage sensing of port 2 and current sensing of ports 2 and 3 was proposed and validated through various tests. The proposed design methodology and control strategy can be applied to any RTPC operating at a wide voltage range at various power levels. As part of future work, the power density of the converter can be analyzed considering the volume and weight of the magnetic components, passives, and heat sinks. In addition, the proposed control strategy can be implemented on the RTPC prototype, validating the effectiveness of the controller.

REFERENCES

[1] *Global EV Outlook 2021*, Int. Energy Agency, Paris, France, 2021.

[2] A. Emadi, Y. J. Lee, and K. Rajashekara, "Power electronics and motor drives in electric, hybrid electric, and plug-in hybrid electric vehicles," *IEEE Trans. Ind. Electron.*, vol. 55, no. 6, pp. 2237–2245, Jun. 2008.

[3] N. Keshmiri, D. Wang, B. Agrawal, R. Hou, and A. Emadi, "Current status and future trends of GaN HEMTs in electrified transportation," *IEEE Access*, vol. 8, pp. 70553–70571, 2020.

[4] H. Krishnaswami and N. Mohan, "Three-port series-resonant dc–dc converter to interface renewable energy sources with bidirectional load and energy storage ports," *IEEE Trans. Power Electron.*, vol. 24, no. 10, pp. 2289–2297, Oct. 2009.

[5] D. Liu and H. Li, "A ZVS bi-directional dc–dc converter for multiple energy storage elements," *IEEE Trans. Power Electron.*, vol. 21, no. 5, pp. 1513–1517, Sep. 2006.

[6] M. I. Marei, B. N. Alajmi, I. Abdelsalam, and N. A. Ahmed, "An integrated topology of three-port dc-dc converter for PV-battery power systems," *IEEE Open J. Ind. Electron. Soc.*, vol. 3, pp. 409–419, 2022.

[7] H. Tao, A. Kotsopoulos, J. L. Duarte, and M. A. M. Hendrix, "Transformer-coupled multiport ZVS bidirectional dc–dc converter with wide input range," *IEEE Trans. Power Electron.*, vol. 23, no. 2, pp. 771–781, Mar. 2008.

[8] J. Schäfer, D. Bortis, and J. W. Kolar, "Multi-port multi-cell dc/dc converter topology for electric vehicle's power distribution networks," in *Proc. IEEE 18th Workshop Control Model. Power Electron.*, 2017, pp. 1–9.

[9] H. Tao, J. L. Duarte, and M. A. M. Hendrix, "High-power three-port three-phase bidirectional dc–dc converter," in *Proc. IEEE Ind. Appl. Annu. Meeting*, 2007, pp. 2022–2029.

[10] S. Inoue, K. Itoh, M. Ishigaki, T. Sugiyama, and M. Sugai, "An isolated three-port dc–dc converter with high power density in 10 cm × 5 cm × 0.8 cm card size for flexible automotive systems," in *Proc. IEEE Energy Convers. Congr. Expo.*, 2016, pp. 1–8.

[11] M. Michon, J. Duarte, M. Hendrix, and M. Simoes, "A three-port bi-directional converter for hybrid fuel cell systems," in *Proc. IEEE 35th Annu. Power Electron. Spec. Conf.*, 2004, vol. 6, pp. 4736–4742.

[12] H. Tao, A. Kotsopoulos, J. Duarte, and M. Hendrix, "A soft-switched three-port bidirectional converter for fuel cell and supercapacitor applications," in *Proc. IEEE 36th Power Electron. Spec. Conf.*, 2005, pp. 2487–2493.

[13] N. D. Dao, D.-C. Lee, and Q. D. Phan, "High-efficiency SiC-based isolated three-port dc/dc converters for hybrid charging stations," *IEEE Trans. Power Electron.*, vol. 35, no. 10, pp. 10455–10465, Oct. 2020.

[14] Y. Wang, F. Han, L. Yang, R. Xu, and R. Liu, "A three-port bidirectional multi-element resonant converter with decoupled power flow management for hybrid energy storage systems," *IEEE Access*, vol. 6, pp. 61331–61341, 2018.

[15] P. Wang, X. Lu, W. Wang, and D. Xu, "Hardware decoupling and autonomous control of series-resonance-based three-port converters in DC microgrids," *IEEE Trans. Ind. Appl.*, vol. 55, no. 4, pp. 3901–3914, Jul./Aug. 2019.

[16] S. Mukherjee, A. Kumar, and S. Chakraborty, "Comparison of DAB and LLC dc–dc converters in high-step-down fixed-conversion-ratio (DCX) applications," *IEEE Trans. Power Electron.*, vol. 36, no. 4, pp. 4383–4398, Apr. 2021.

[17] K. Wang, W. Liu, and F. Wu, "Topology-level power decoupling three-port isolated current-fed resonant dc–dc converter," *IEEE Trans. Ind. Electron.*, vol. 69, no. 5, pp. 4859–4868, May 2022.

[18] Y.-K. Tran, F. D. Freijedo, and D. Dujic, "Open-loop power sharing characteristic of a three-port resonant LLC converter," *CPSS Trans. Power Electron. Appl.*, vol. 4, no. 2, pp. 171–179, 2019.

[19] J. Deng, S. Li, S. Hu, C. C. Mi, and R. Ma, "Design methodology of LLC resonant converters for electric vehicle battery chargers," *IEEE Trans. Veh. Technol.*, vol. 63, no. 4, pp. 1581–1592, May 2014.

[20] J. L. Duarte, M. Hendrix, and M. G. Simoes, "Three-port bidirectional converter for hybrid fuel cell systems," *IEEE Trans. Power Electron.*, vol. 22, no. 2, pp. 480–487, Mar. 2007.

[21] C. Zhao, S. D. Round, and J. W. Kolar, "An isolated three-port bidirectional dc–dc converter with decoupled power flow management," *IEEE Trans. Power Electron.*, vol. 23, no. 5, pp. 2443–2453, Sep. 2008.

[22] J. F. Lazar and R. Martinelli, "Steady-state analysis of the LLC series resonant converter," in *Proc. 16th Annu. IEEE Appl. Power Electron. Conf. Expo.*, 2001, vol. 2, pp. 728–735.

[23] V. Vorperian and S. Cuk, "A complete dc analysis of the series resonant converter," in *Proc. IEEE Power Electron. Spec. Conf.*, 1982, pp. 85–100.

[24] J.-H. Jung, H.-S. Kim, M.-H. Ryu, and J.-W. Baek, "Design methodology of bidirectional CLLC resonant converter for high-frequency isolation of dc distribution systems," *IEEE Trans. Power Electron.*, vol. 28, no. 4, pp. 1741–1755, Apr. 2013.

[25] G. Ke, Q. Chen, S. Zhang, X. Xu, and L. Xu, "A single-ended hybrid resonant converter with high misalignment tolerance," *IEEE Trans. Power Electron.*, vol. 37, no. 10, pp. 12841–12852, Oct. 2022.

[26] S. Sanders, J. Noworolski, X. Liu, and G. Verghese, "Generalized averaging method for power conversion circuits," *IEEE Trans. Power Electron.*, vol. 6, no. 2, pp. 251–259, Apr. 1991.

[27] D. G. Zill, *Advanced Engineering Mathematics*. Boston, MA, USA: Jones & Bartlett Publishers, 2020.

[28] N. S. Nise, *Control System Engineering*. New York, NY, USA: Wiley, 2011.

NILOUFAR KESHMIRI (Student Member, IEEE) received the B.Eng. degree in electrical engineering and management in 2018 from McMaster University, Hamilton, ON, Canada, where she is currently working toward the Ph.D. degree with the McMaster Automotive Resource Centre.

She specializes in high-efficiency converter systems using gallium nitride wide-bandgap semiconductor technology. Her research interests include the design, control, and optimization of power electronics converters in electrified transportation applications.
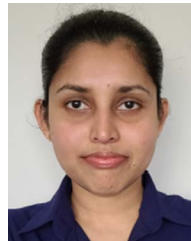
GUVANTHI ABEYSINGHE MUDIYANSELAGE (Student Member, IEEE) received the B.Eng. degree in electrical engineering from the University of Moratuwa, Moratuwa, Sri Lanka, in 2016, and the master's degree in electrical and computer engineering in 2020 from McMaster University, Hamilton, ON, Canada, where she is currently working toward the Ph.D. degree, focusing on the development of power electronics dc–dc converters for electrified transportation applications, in 2021.

SREEJITH CHAKKALAKKAL (Student Member, IEEE) received the B.Eng. degree in electrical and electronics engineering from the University of Calicut, Malappuram, India, in 2009, and the M.Tech. degree in electrical engineering from the Indian Institute of Technology, Kanpur, India, in 2013. He is currently working toward the Ph.D. degree with the Department of Electrical and Computer Engineering, McMaster University, Hamilton, ON, Canada.

From 2013 to 2021, he was an Engineer with the Eaton India Innovation Center, Pune, India. His research interests include high-power-density dc–dc converters and integrated high-frequency magnetics.
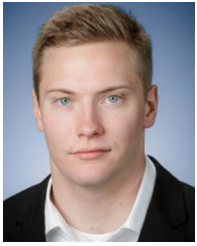
KYLE KOZIELSKI (Student Member, IEEE) received the B.Eng. degree in electrical engineering in 2022 from McMaster University, Hamilton, ON, Canada, where he is currently working toward the M.A.Sc. degree with the McMaster Automotive Resource Centre.

His research interests include power electronics converters and solid-state protection circuits in electrified transportation applications.

GIORGIO PIETRINI (Member, IEEE) received the B.Sc., M.Sc., and the Ph.D. degrees in information technology from the Department of Information Engineering, University of Parma, Parma, Italy, in 2009, 2014, and 2019, respectively.

In May 2019, he joined the McMaster Automotive Resource Centre (MARC), McMaster University, Hamilton, ON, Canada, as a Post-Doctoral Fellow. His main research interests include electrical machine design and modeling with special regard to permanent magnet synchronous motors for high-performance automotive traction and aerospace applications.

ALI EMADI (Fellow, IEEE) received the B.S. and M.S. degrees in electrical engineering with highest distinction from the Sharif University of Technology, Tehran, Iran, in 1995 and 1997, respectively, and the Ph.D. degree in electrical engineering from Texas A&M University, College Station, TX, USA, in 2000.

He is currently the Canada Excellence Research Chair Laureate with McMaster University, Hamilton, ON, Canada. He is also the holder of the NSERC/FCA Industrial Research Chair in Electrified Powertrains and Tier I Canada Research Chair in Transportation Electrification and Smart Mobility. Before joining McMaster University, he was the Harris Perlstein Endowed Chair Professor of Engineering and the Director of the Electric Power and Power Electronics Center and Grainger Laboratories, Illinois Institute of Technology, Chicago, IL, USA, where he established research and teaching facilities as well as courses in power electronics, motor drives, and vehicular power systems. He was the Founder, Chairman, and President of Hybrid Electric Vehicle Technologies, Inc.—a university spin-off company of the Illinois Institute of Technology. He is the President and Chief Executive Officer of Enedym, Inc. and Menlolab, Inc.—two McMaster University spin-off companies. He is the principal author/coauthor of more than 500 journal and conference papers as well as several books including *Vehicular Electric Power Systems* (Boca Raton, FL, USA: CRC Press, 2003), *Energy-Efficient Electric Motors* (New York, NY, USA: Taylor & Francis, 2004), *Uninterruptible Power Supplies and Active Filters* (Boca Raton, FL, USA: CRC Press, 2004), *Modern Electric, Hybrid Electric, and Fuel Cell Vehicles* (2nd ed. Boca Raton, FL, USA: CRC Press, 2009), and *Integrated Power Electronic Converters and Digital Control* (Boca Raton, FL, USA: CRC Press, 2009). He is also the Editor for the books titled *Handbook of Automotive Power Electronics and Motor Drives* (Boca Raton, FL, USA: CRC Press, 2005) and *Advanced Electric Drive Vehicles* (Boca Raton, FL, USA: CRC Press, 2014). He is the co-editor for the book titled *Switched Reluctance Motor Drives* (Boca Raton, FL, USA: CRC Press, 2018).

Dr. Emadi was the Inaugural General Chair of 2012 IEEE Transportation Electrification Conference and Expo and has chaired several IEEE and SAE conferences in the areas of vehicle power and propulsion. He was the founding Editor-in-Chief for the IEEE TRANSACTIONS ON TRANSPORTATION ELECTRIFICATION from 2014 to 2020.